ADVANCED MATERIALS
www.advmat.de

Combining Efficiency and Stability in Mixed Tin–Lead Perovskite Solar Cells by Capping Grains with an Ultrathin 2D Layer

Mingyang Wei, Ke Xiao, Grant Walters, Renxing Lin, Yongbiao Zhao, Makhsud I. Saidaminov, Petar Todorović, Andrew Johnston, Ziru Huang, Haijie Chen, Aidong Li, Jia Zhu, Zhenyu Yang, Ya-Kun Wang, Andrew H. Proppe, Shana O. Kelley, Yi Hou, Oleksandr Voznyy, Hairen Tan, and Edward H. Sargent**

The development of narrow-bandgap ($E_g \approx 1.2$ eV) mixed tin–lead (Sn–Pb) halide perovskites enables all-perovskite tandem solar cells. Whereas pure-lead halide perovskite solar cells (PSCs) have advanced simultaneously in efficiency and stability, achieving this crucial combination remains a challenge in Sn–Pb PSCs. Here, Sn–Pb perovskite grains are anchored with ultrathin layered perovskites to overcome the efficiency-stability tradeoff. Defect passivation is achieved both on the perovskite film surface and at grain boundaries, an approach implemented by directly introducing phenethylammonium ligands in the antisolvent. This improves device operational stability and also avoids the excess formation of layered perovskites that would otherwise hinder charge transport. Sn–Pb PSCs with fill factors of 79% and a certified power conversion efficiency (PCE) of 18.95% are reported—among the highest for Sn–Pb PSCs. Using this approach, a 200-fold enhancement in device operating lifetime is achieved relative to the nonpassivated Sn–Pb PSCs under full AM1.5G illumination, and a 200 h diurnal operating time without efficiency drop is achieved under filtered AM1.5G illumination.

Metal halide perovskites are attractive photovoltaic materials in view of their excellent optoelectronic properties and ease of fabrication.[1–4] For single-junction perovskite solar cells (PSC), a certified power conversion efficiency of 25.2% has been reported,[5] approaching the performance levels of silicon solar cells. With the goal of further improving power conversion efficiency (PCE), researchers have fabricated all-perovskite tandem solar cells that provide an avenue ultimately to exceed the Shockley–Queisser limit,[6–11] the theoretical upper limit to PCE of single-junction solar cells.

A typical all-perovskite tandem solar cell is comprised of a front cell that utilizes a wide-bandgap ($E_g \approx 1.7$–1.8 eV) lead mixed-halide perovskite; and a back cell based on a narrow-bandgap ($E_g \approx 1.2$ eV) mixed tin–lead (Sn–Pb) iodide perovskite. The best performing two-terminal tandem PSC has been reported to have a PCE of 24.8%.[7]

Achieving the needed performance × stability combination in Sn–Pb PSCs has become the bottleneck to further progress in all-perovskite tandem solar cells. Formamidinium (FA) and methylammonium (MA) mixed-cation Sn–Pb PSCs now exceed 18% PCE, with a highest value of 21.1% reported.[7,10–14] The corresponding Sn–Pb PSCs typically have a limited operating lifetime. In contrast, FA and cesium (Cs) based Sn–Pb PSCs have exhibited excellent thermal and over 500-hour

M. Wei, Dr. G. Walters, Dr. Y. Zhao, Prof. M. I. Saidaminov,[+]
P. Todorović, A. Johnston, Z. Huang, Dr. H. Chen, Prof. Z. Yang,
Y.-K. Wang, Dr. A. H. Proppe, Dr. Y. Hou, Prof. O. Voznyy,
Prof. E. H. Sargent
Department of Electrical and Computer Engineering
University of Toronto
Toronto, Ontario M5S 3G4, Canada
E-mail: ted.sargent@utoronto.ca

The ORCID identification number(s) for the author(s) of this article can be found under https://doi.org/10.1002/adma.201907058.

[+]Present address: Department of Chemistry and Electrical & Computer Engineering, Centre for Advanced Materials and Related Technologies (CAMTEC), University of Victoria, 3800 Finnerty Rd, Victoria, BC V8P 5C2, Canada

DOI: 10.1002/adma.201907058

K. Xiao, R. Lin, Prof. A. Li, Prof. J. Zhu, Prof. H. Tan
National Laboratory of Solid State Microstructures
Jiangsu Key Laboratory of Artificial Functional Materials
College of Engineering and Applied Sciences
Nanjing University
Nanjing 210093, China
E-mail: hairentan@nju.edu.cn

Dr. A. H. Proppe, Prof. S. O. Kelley
Department of Chemistry
University of Toronto
80 St. George Street, Toronto, Ontario M5S 3G4, Canada

Prof. S. O. Kelley
Department of Pharmaceutical Sciences
Leslie Dan Faculty of Pharmacy
University of Toronto
Toronto, Ontario M5S 3M2, Canada

operating stability, but their PCE (single junction < 17%) has curtailed tandems based on this approach.[15,16]

Incorporation of layered perovskites to form 2D/3D hybrid structures is a promising approach to resolve this dilemma, as seen in lead-based PSCs.[17–21] Layered perovskites have the chemical formula of $A_2(FA/MA/Cs)_{n-1}(Pb/Sn)_n(Br/I)_{3n+1}$, where A is the bulky organic cation attached to the corner-sharing $[PbI_6]$ or $[SnI_6]$ octahedral framework. Compared with 3D perovskites, layered perovskites have increased resistance to both intrinsic and extrinsic degradation.[17,18] For pure-Pb PSCs, active layers comprised of 3D perovskites terminated with a thin layered perovskite layer on the hole transport layer (HTL) or electron transport layer (ETL) side have enabled stable and efficient devices.[18,20,21]

Until now, the conventional 2D/3D strategy has not translated into both stable and efficient Sn–Pb PSCs.[19,22–24] It can increase stability in Sn–Pb devices, but such an excess of bulky organic cation was required that a low fill-factor (FF < 70%) was obtained—presumably arising from blocked out-of-plane carrier transport in layered perovskites.[25,26]

We reasoned that the limited performance and stability of Sn–Pb perovskites could originate from high defect densities (e.g., Sn^{2+} vacancies) on the surface of grains (film surface and grain-boundaries).[7,11,12] We posited that anchoring, onto Sn–Pb perovskite grains, layered perovskites—but avoiding the excess formation of the layered phase which would block the charge carrier transport—could therefore enable simultaneous improvements in device efficiency and stability through passivation of the defects.[27]

Here we employed the bulky organic cation phenethylammonium (PEA) to anchor the Sn–Pb perovskite grains. By introducing the PEA cation directly into the antisolvent, we achieved in situ defect passivation both at the perovskite film surface, and at grain boundaries within the film; yet we also avoided the excess formation of layered perovskite phases. Using this approach, we achieved a 200-fold enhancement in device operating lifetime over the nonpassivated Sn–Pb PSCs under full AM1.5G illumination, and no efficiency drop following 200 h of diurnal device operation under filtered AM1.5G illumination. We preserved a high fill factor of 79%, leading to a lab-measured PCE of 19.4% (certified 18.95%). We then demonstrated efficient two-terminal all-perovskite tandem solar cells that employ the PEA-anchored Sn–Pb PSC as the back subcell. We obtained a stabilized PCE of 23.5% for the tandem cells.

We fabricated triple-cation FA/MA/Cs Sn–Pb perovskites to investigate defect passivation via the introduction of the bulky organic cation. Here the Sn/Pb element ratio was set to 1:1 in the precursor mixture, and the resultant perovskite films have a bandgap of 1.25 eV (Figure S1, Supporting Information).[6,9–12] X-ray diffraction (XRD) reveals a pseudo-cubic structure for the Sn–Pb perovskite films (Figure S2a, Supporting Information), without evidence of a yellow phase. An additional peak at 10° was attributed to the PbI_2/SnI_2–DMSO complex, present as a result of the short annealing time (Figure S3, Supporting Information). The perovskite film is smooth and pinhole-free, with an average grain size of 600 nm, as revealed using scanning electron microscopy (SEM) (**Figure 1**a).

We dissolved PEA at a low concentration (0.5 mg mL^{-1}) using phenethylammonium iodide in ethyl acetate (EA), and then used this solution to post-treat the perovskite film surface. We term this approach the surface-passivation method (**Figure 2**a).

The surface morphology of the surface-passivated perovskites remains the same as that of the pristine perovskites (Figure 1b). No changes in XRD patterns were observed for the surface-passivated perovskites (Figure S2b, Supporting Information). The presence of PEA cation was investigated using time-of-flight secondary ion mass spectrometry (ToF-SIMS). The highest PEA presence was detected nearer the front surface of the perovskite film (Figure S4, Supporting Information), while it rapidly decreased within the film. We conclude that PEA does not penetrate deeply into the bulk of the perovskite film.

We then acquired grazing-incidence wide-angle X-ray scattering (GIWAXS) data to characterize the structure of perovskites. The incidence angle was set as low as 0.5° to probe the surface structure.[28] As shown in Figure 2c and Figure S5a (Supporting Information), the main diffraction peaks from the pristine perovskite film are assigned to the polycrystalline 3D perovskite.[29] After the post-treatment, the film preserves the 3D perovskite structure (Figure S5b, Supporting Information), and no additional small-angle XRD peaks (belonging to layered phase) appear (Figure 2c). This absence of scattering below 6 nm^{-1} indicates no detectable layered perovskite domains at the top surface of the surface-passivated film.[30]

We further investigated the phase distribution of perovskites on the very upper surface via ultrafast transient reflection (TR) spectroscopy. As seen in Figure S6a (Supporting Information), two antisymmetric peaks in the near-infrared region were found for the pristine perovskites, corresponding to the ground-state bleach. Additionally, a negative feature was observed at 550 nm, which arises from the high energy band bleach.[31] For surface-passivated perovskite films (Figure 1d and Figure S6b, Supporting Information), the shape of TR spectra remains similar to that of pristine perovskites, without distinct peaks appearing from a layered perovskite phase (Figure S7a, Supporting Information).[30–32] Combining the GIWAXS and TR studies, we conclude that layered perovskite domains were below the detection limit for the surface-passivated films in these studies.

With the goal of understanding how phenethylammonium iodide (PEAI) interacts with the perovskite surface, we increased the thickness of the PEAI passivation layer until we could reach detectable signals. Upon increasing the PEAI concentration to 1.5 mg mL^{-1}, we found a negative feature associated with the $n = 1$ layered perovskite (2D perovskite) in the TR spectra (Figure S7b,c, Supporting Information). The 2D perovskite formation was confirmed by the appearance of related diffraction peaks in the XRD spectra, while no diffraction peaks stemming from the PEAI aggregates were observed (Figure S7d, Supporting Information). This suggests that the PEAI led to 2D perovskites on the film surface. We expect that the diminishing of the 2D perovskite signal for the surface passivated film is a result of an ultrathin passivation layer formed on the surface. This ultrathin passivation layer enables surface defect passivation while maintaining efficient charge extraction.

We then utilized the X-ray photoelectron spectroscopy (XPS) to study the capacity of 2D perovskite layers to provide passivation. We found that the surface passivation method reduces the oxidation of perovskites. This was evidenced by the reduced

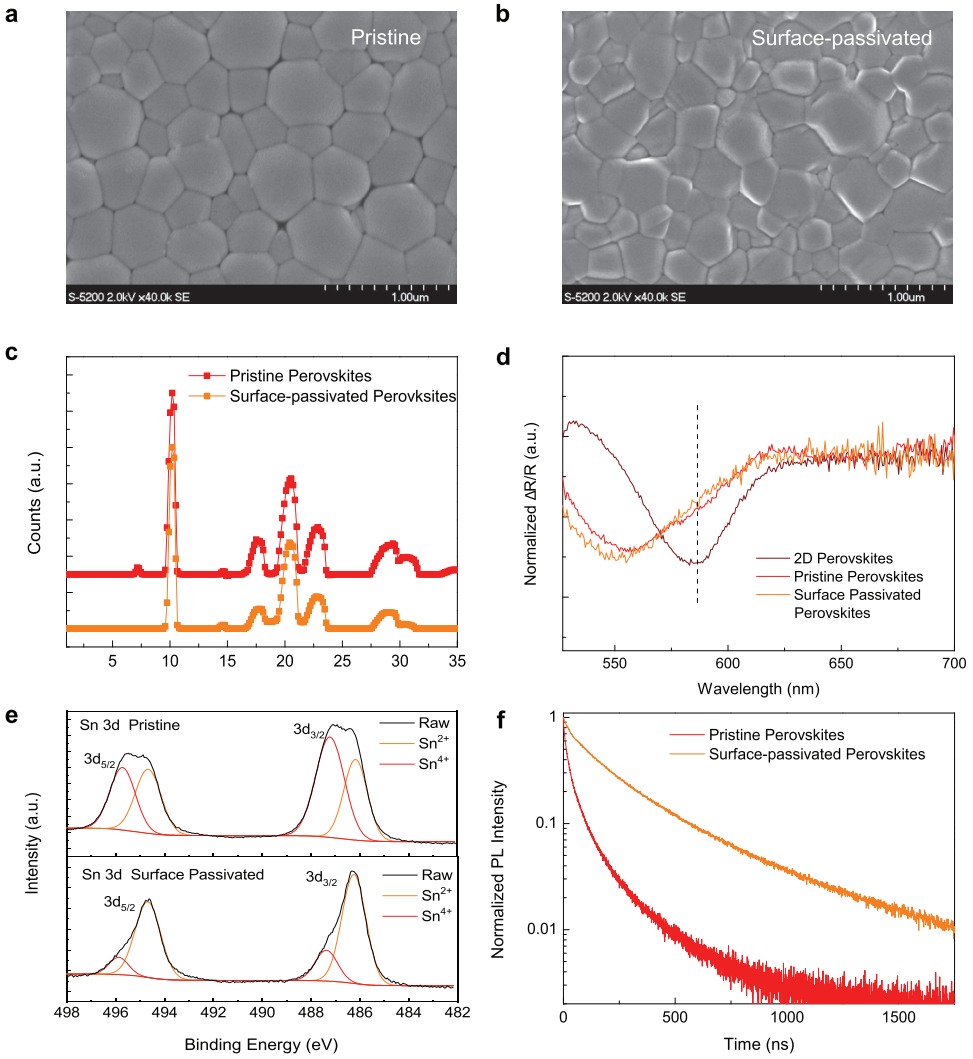

Figure 1. Structure and carrier dynamics of phenethylammonium (PEA) cation-surface passivated tin–lead (Sn–Pb) perovskites. Top-view scanning electron microscope (SEM) images of the a) pristine and b) surface-passivated perovskite films deposited on PEDOT:PSS-coated ITO substrates. The film morphology remains similar for the two films. c) Cuts near the q_z axis of grazing-incidence wide-angle X-ray scattering (GIWAXS) measurements. The surface-passivated perovskites preserve the 3D perovskite structure without the formation of layered phases. d) Transient reflection (TR) spectra of the 2D perovskites, pristine perovskites, and surface-passivated perovskites, after 1 ps of pump–probe delay. The spectra feature of the layered perovskite phase is not observed for the surface-passivated perovskites. e) The Sn 3d X-ray photoelectron spectroscopy (XPS) spectra of the pristine and surface-passivated perovskites. The Sn^{4+} formation is reduced for the surface-passivated perovskites. f) Time-resolved photoluminescence (PL) decay of perovskite films probed from the top side of the samples. Prolonged carrier lifetime is observed for the surface-passivated perovskites.

Sn^{4+} signal in the Sn 3d spectra (Figure 1d). The hydrophobic PEA cation suppresses the diffusion of moisture, as indicated by the reduced C=O bond signal in the C 1s spectra for the surface-passivated perovskites (Figure S8, Supporting Information). These results suggest that even a limited amount of formation of the 2D phase on the film surface can contribute to reduced defect densities in Sn–Pb perovskites.

We further employed time-resolved photoluminescence (TR-PL) measurements to study carrier recombination dynamics. An PL decay lifetime of 32 ns was obtained for the pristine perovskites (Figure 1e), indicative of severe nonradiative carrier recombination within the untreated perovskite film. Following PEA cation passivation, the PL lifetime is extended to 210 ns, approaching that of pure-Pb perovskites.[33,34]

We compared the surface passivation method with the conventional post-treatment method.[18,27,28] We found that the conventional isopropanol (IPA) based post-treatment can induce surface degradation (Figure S9a, Supporting Information). As a result, a thin passivation layer (Figure S9b, Supporting Information) is not sufficient to reduce carrier trapping for the IPA-based post-treatment method (Figure S9c, Supporting Information).

For the surface-passivated Sn–Pb perovskite films, a longer PL lifetime was seen only when we probed the PL signal from the front (treated) side of the perovskite film (Figure 2d). When the TR-PL decay was probed from the glass (less treated) side of the perovskite film, the decay rate remained as fast as in the untreated pristine samples. We attribute this short PL lifetime

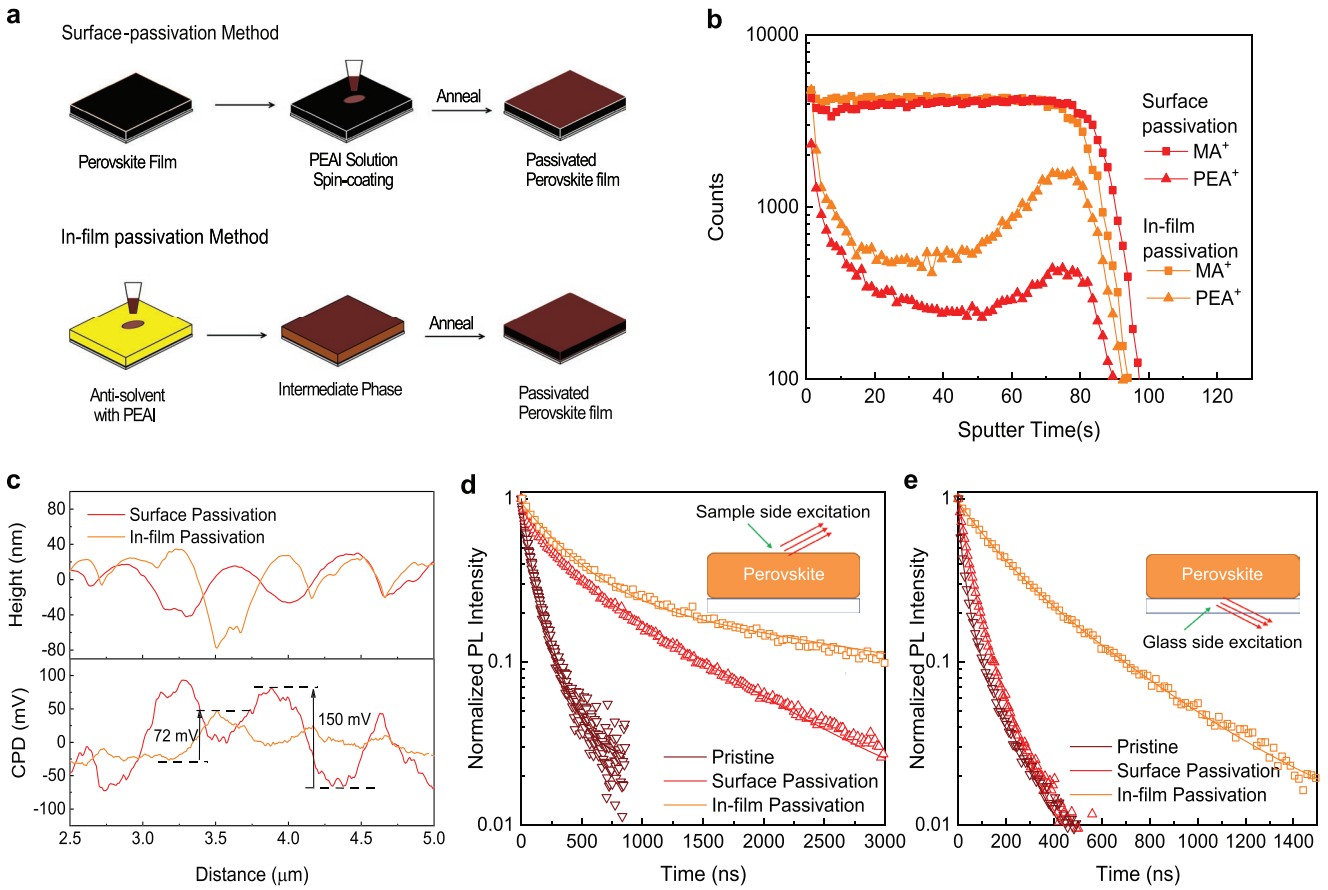

Figure 2. In-film passivation of Sn–Pb perovskite films. a) Schematics of processing methods to achieve surface-passivation or in-film passivation (passivation for both film surface and grain boundaries). b) Time-of-flight secondary ion mass spectrometry (ToF-SIMS) depth profiles of the surface-passivated and in-film passivated perovskite films. A significantly higher amount of PEA cation is found within the bulk film for the in-film passivated sample. c) Topography and relative contact potential difference (CPD) line-scan spectra for the surface-passivated and in-film passivated perovskite films. These indicate more homogeneous CPD distributions for the in-film passivated perovskite films. Time-resolved PL decay of perovskite films from d) the top side or from e) the glass side of the samples.

probed from the glass side to the limited penetration depth of the PEA cation during the surface treatment (Figure 2a and Figure S4, Supporting Information).

We then turned instead to using PEAI in EA as the anti-solvent for perovskite fabrication: this, we speculated, might enable ligand anchoring occurs on both the film surface and also at grain boundaries within the bulk film. We term these samples in-film passivated (Figure 2a). The films exhibited substantially the same surface morphology and crystalline structure (Figure S10, Supporting Information) of the surface-passivated perovskites. GIWAXS (Figure S11, Supporting Information) and TR studies (Figure S12, Supporting Information) indicate that the layered perovskite phase is too thin to be detected when the in-film passivation method is employed—just as seen in the surface-passivation method. The thin passivation layer is still sufficient to reduce defect densities (Figure S13, Supporting Information).[35,36]

The spatial distribution of PEA cations within the perovskite films produced using different passivation methods was investigated using ToF-SIMS (Figure 2b). For the in-film passivation method, a significantly higher signal of PEA ligands was detected compared to the case of the surface-passivation method. The in-film passivation approach enables deeper penetration of PEA cations into the whole film. This in-film passivation approach, we propose, is capable of passivating grain boundaries inside the bulk of the film, in addition to passivating the top surface of the perovskite films.

We then characterized grain boundary passivation with the aid of Kelvin probe force microscopy (KPFM). An average surface potential difference between the grain boundary and the adjacent grain interior of 72 and 75 mV was found for the pristine and surface passivated perovskites, respectively (Figures S14a–b and S15, Supporting Information). This indicates the charge carrier trapping happens at the grain boundaries, consistent with previous reports.[11,12] For the in-film passivated perovskites, this average surface potential difference is significantly reduced to 39 mV (Figure S15, Supporting Information). Since the surface morphology remained similar for all perovskite films (Figure S14d, Supporting Information and Figure 2c), we propose that deep penetration of PEAI within perovskite films can passivate grain boundaries to reduce the charge carrier trapping. This leads to a prolonged PL lifetime probed from each side (top and bottom) of the in-film passivated film (Figure 2d,e). The PL intensity of the in-film

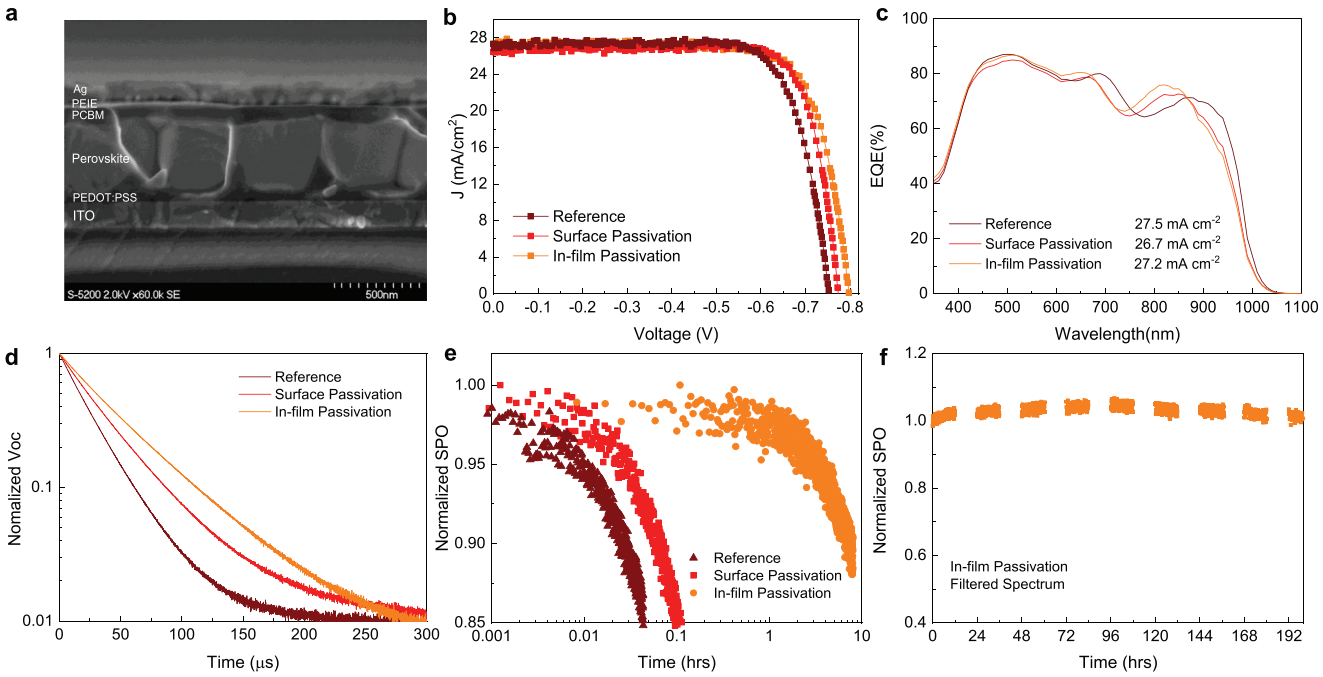

Figure 3. Improved efficiency and stability of in-film passivated Sn–Pb perovskite solar cells. a) Cross-sectional SEM image of the Sn–Pb PSC with an inverted device structure. b) Current density–voltage (*J*–*V*) curves of Sn–Pb perovskite solar cells fabricated with pristine, surface-passivation, and in-film passivation methods. c) External quantum efficiency (EQE) spectra and integrated short-circuit current density (J_{SC}) values of corresponding Sn–Pb perovskite solar cells. d) Transient photovoltage decay curves of Sn–Pb perovskite solar cells. Long-term maximum power point tracking of the Sn–Pb solar cells under e) full AM1.5G illumination and under f) illumination filtered by a wide-bandgap perovskite film.

passivated perovskite film is also stronger (Figure S16b,c, Supporting Information) compared with the surface-passivated perovskite film and the pristine perovskite film.

We fabricated Sn–Pb PSCs having the inverted structure: indium-doped tin oxide (ITO)/poly(3,4-ethylenedioxythiophene):polystyrene sulfonate (PEDOT:PSS) (50 nm)/Sn–Pb perovskite (400 nm)/phenyl-C_{61}-butyric acid methyl ester (PCBM) (100 nm)/polyethylenimine ethoxylated (PEIE)/Ag (120 nm) (**Figure 3**a). The current density–voltage (*J*–*V*) curves of the champion cells recorded under reverse voltage scanning using each method are presented in Figure 3b. The PCE under forward (reverse) voltage scan is improved from 14.2% (15.3%) to 15.3% (16.7%) for the surface-passivated devices and to 16.2% (16.3%) for the in-film passivated devices. Figure 3c shows the external quantum efficiency (EQE) spectra of the champion cells. Their integrated J_{sc} values match well with those obtained from the *J*–*V* scans. As seen in Table S1 (Supporting Information), the PCE improvement by the PEA cation passivation comes from an increased open-circuit voltage which we associate with defect passivation; and increased FF that we assign further to the minimal formation of carrier-retarding layered perovskite.[27,37–39] The FF (76%) obtained here is higher than that for the layered perovskite-based Sn–Pb PSCs (below 70%).[19,22]

We found that only in-film passivation significantly reduced hysteresis in the JV-scans (Figure S17a, Supporting Information). Steady-state power outputs were tracked for the three classes of devices (Figure S17b, Supporting Information). In-film passivated PSC achieved a stabilized PCE of 16.3%, and the stabilized power output (SPO) is consistent with the *J*–*V* scans. For the pristine and surface-passivated devices, continuous performance decays were observed; thus, we could not reliably extract the SPOs.

We then carried out transient photovoltage (TPV) decay characterization to study carrier recombination dynamics.[40] The TPV decay lifetimes of the passivated PSCs (35 and 45 μs for the surface-passivation method and the in-film passivation method, respectively) are much longer than those of the non-passivated device (25 μs for the reference cell) (Figure 3d). The prolonged lifetimes indicate that each passivation method suppresses nonradiative carrier recombination, accounting for the improved V_{oc} in each passivation method. More effective grain-boundary passivation via the in-film method enables the longest TPV decay lifetime and the highest V_{oc} values among all the devices in this work.

We carried out operational stability measurements of the Sn–Pb PSCs. During maximum power point (MPP) tracking for devices under full AM1.5G illumination (100 mW cm^{-2}, and without UV-filter), the pristine and surface-passivated devices degraded rapidly. Their PCEs dropped to 90% of their initial PCEs (T_{90}) after 1.8 and 4.3 min, respectively (Figure 3e). In comparison, the in-film passivated PSCs exhibited a T_{90} of 8.6 h, which represents an over 200-fold enhancement in the operational lifetime compared with the nonpassivated PSCs. To exclude degradation of PEDOT:PSS induced by long-term UV illumination,[41] we then placed the in-film passivated Sn–Pb PSC under a wide-bandgap (E_g = 1.75 eV) perovskite film (similar to the working conditions present within all-perovskite tandem solar cells). A diurnal test was conducted to emulate solar cell working conditions (Figure 3f; performance of initial

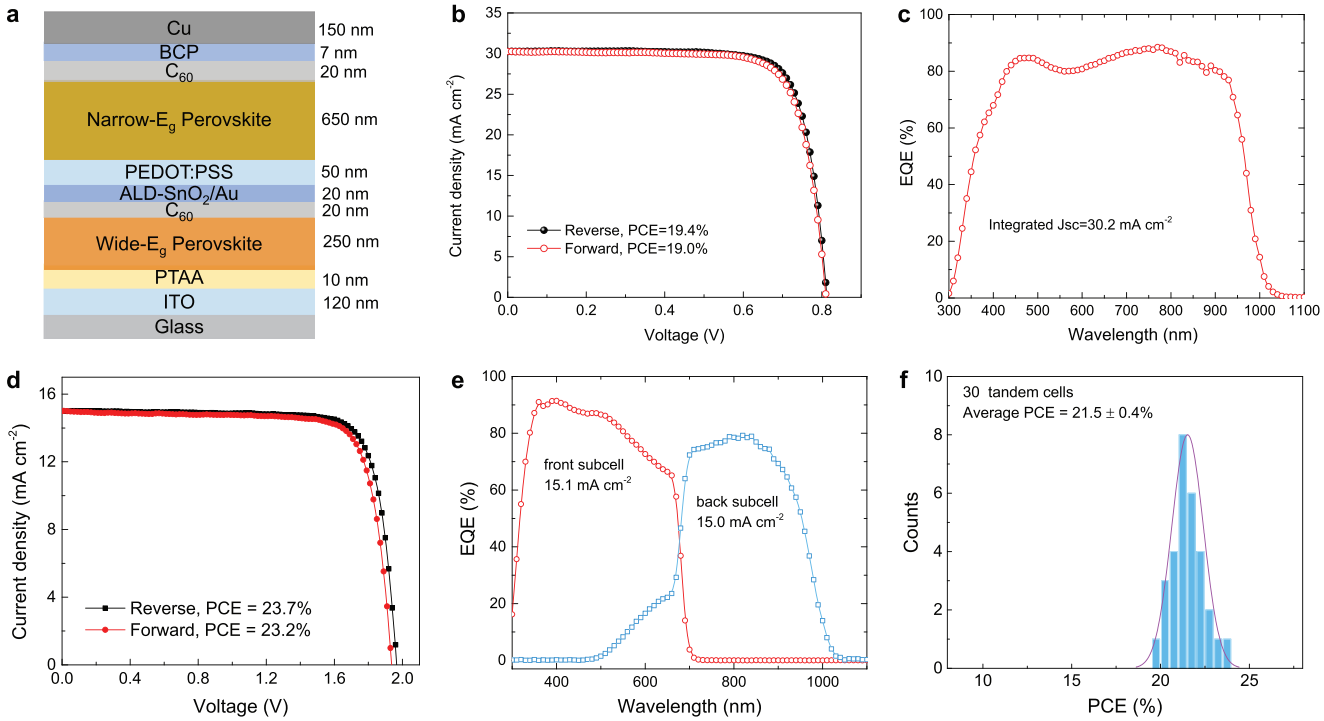

Figure 4. Performance and stability of two-terminal all-perovskite tandem solar cells. a) Device structure of two-terminal all-perovskite solar cells. b) *J–V* and c) EQE curves of the best-performing single-junction Sn–Pb perovskite solar cell with a thicker absorber layer (≈650 nm). d) *J–V* curves, e) EQE spectra of the best-performing two-terminal all-perovskite tandem solar cell. f) Histogram of PCEs for 30 two-terminal all-perovskite tandem solar cells, exhibiting an average PCE of 21.5%.

devices is shown in Figure S18 in the Supporting Information), and these devices retained their initial value following 200 h of testing. The significantly improved device lifetime, as well as the device efficiency for the in-film passivated Sn–Pb PSCs, indicates that the PEA cation anchoring on the film surface and at grain boundaries is required to ensure performance and stability in the Sn–Pb perovskite solar cells studied herein.

We then combined the in-film passivated mixed Sn–Pb narrow-bandgap perovskite with a wide-bandgap perovskite to construct two-terminal all-perovskite tandem solar cells (**Figure 4**a and Figure S19, Supporting Information). Here we adopted a thick absorber layer (≈650 nm) in mixed Sn–Pb PSCs to enable sufficient light absorption. We replaced the solution-processed PCBM/PEIE bilayer with a thermally evaporated C_{60}/BCP bilayer as the ETL to ensure conformal surface coverage. PCEs of 19.4% and 19.0% were obtained in the best-performing Sn–Pb single-junction PSCs under reverse and forward scans (Figure 4b), respectively, while the pristine Sn–Pb perovskites achieve a best PCE of 17.9% (Figure S20, Supporting Information) under reverse scan. The in-film passivated Sn–Pb PSCs exhibited minimal performance degradation following 1-month storage in a N_2-filled glovebox (Figure S21, Supporting Information). As in the thin devices shown in Figure 3b, the thick in-film passivated Sn–Pb PSCs show substantially improved performance compared with control devices (Figure S22, Supporting Information). The J_{sc} values obtained from *J–V* measurements match with the integrated J_{sc} (≈30.2 mA cm^{-2}) from EQE spectra (Figure 4c). This high J_{sc} value was achieved here for an active layer thickness below 700 nm, a fact that may be assigned to improved charge transport and carrier extraction thanks to in-film passivation via PEA cations. We also find that this method can be applied using the *n*-butylammonium cation (Figure S23, Supporting Information). We sent one device to Newport (Montana, USA) for independent characterization, and this device achieved a certified PCE of 18.95% (Figure S24, Supporting Information)—competitive among high-efficiency Sn–Pb PSCs (Tables S2 and S3, Supporting Information). The J_{sc} values measured at Newport are consistent with in-lab measurements (Table S4, Supporting Information). When we further increased the active layer thickness to 1 µm, the in-film passivation method remained effective (Figure S25, Supporting Information).

We used atomic layer deposited (ALD) SnO_2 (20 nm) as the interconnection layer (ICL) for connecting the two subcells (Figure 4a). A thin Au layer (≈1–2 nm) was inserted to ensure charge recombination between subcells. The champion PCE for the tandem PSCs (Figure 4d and **Table 1**) is 23.7%, with a J_{sc} of 15.0 mA cm^{-2}, FF of 80.4%, and V_{oc} of 1.967 V under reverse scan. The tandem solar cell exhibits low hysteresis (PCE = 23.2% under forward scan) in *J–V* scans and has a stabilized PCE of 23.5% (Figure S26, Supporting Information). The EQE spectra (Figure 4e) show integrated J_{sc} values of 15.1 and 15.0 mA cm^{-2} for the front and back subcells, respectively, matching well with the J_{sc} values from *J–V* measurements. We fabricated 30 tandem solar cells, and the devices showed a narrow PCE distribution (Figure 4f).

We further performed operational stability tests for the tandem PSCs. The devices retained 95% of their initial value

Table 1. Photovoltaic performance of two-terminal (2T) all-perovskite tandem solar cells and corresponding subcells.

Cells	Scan direction	V_{oc} [V]	J_{sc} [mA cm^{-2}]	FF [%]	PCE [%]
Wide bandgap front subcell	Reverse	1.211	17.3	76.8	16.1
	Forward	1.192	17.4	77.1	16.0
Narrow bandgap back subcell	Reverse	0.813	30.3	78.9	19.4
	Forward	0.811	30.3	77.4	19.0
2T tandem	Reverse	1.967	15.0	80.4	23.7
	Forward	1.937	15.0	79.4	23.2

following 65 h of operation at MPP under AM1.5G illumination (Figure S27, Supporting Information).

In summary, we developed ligand anchored Sn–Pb perovskites to seek simultaneous improvements in device efficiency and stability within narrow-bandgap PSCs. We employed PEA cations as anchoring ligands, and these suppressed nonradiative carrier recombination in Sn–Pb perovskite active layers. We developed a fabrication method that passivates both the perovskite film surface and the grain boundaries, yet avoids the excess formation of layered perovskite phase that would otherwise block carrier transport. This approach enables a 200-fold improvement in the mixed Sn–Pb PSC operating lifetime over the nonpassivated Sn–Pb PSCs and a PCE of 19.4% (certified 18.95%) for the thick Sn–Pb PSCs. We then demonstrated monolithic all-perovskite tandem solar cells using PEA-anchored Sn–Pb PSCs as back cells. We achieved a stabilized PCE of 23.5% for tandem PSCs. The work indicates that passivating defects on film surfaces and at grain boundaries enables efficient and stable Sn–Pb perovskite solar cells.

Supporting Information

Supporting Information is available from the Wiley Online Library or from the author.

Acknowledgements

M.W. and K.X. contributed equally to this work. This publication was based in part on work supported by the US Office of Naval Research (Grant Award No.: N00014-17-1-2524), by an award (OSR-2017-CPF-3321-03) from the King Abdullah University of Science and Technology (KAUST), by the Ontario Research Fund Research Excellence Program, and by the Natural Sciences and Engineering Research Council (NSERC) of Canada. The work of H.T. was supported by National Key R&D Program of China (Grant No. 2018YFB1500102), the National Natural Science Foundation of China (Grant No. 61974063), the Jiangsu Provincial Natural Science Foundation (BK20190315), and the Thousand Talent Program for Young Outstanding Scientists in China. M.I.S. acknowledges the Government of Canada's Banting Postdoctoral Fellowship Program for financial support.

Conflict of Interest

The authors declare no conflict of interest.

Keywords

layered perovskites, passivation, Sn–Pb perovskite solar cells, tandem perovskite solar cells

Received: October 28, 2019
Revised: January 2, 2020
Published online:

[1] S. D. Stranks, H. J. Snaith, *Nat. Nanotechnol.* **2015**, *10*, 391.
[2] N.-G. Park, M. Grätzel, T. Miyasaka, K. Zhu, K. Emery, *Nat. Energy* **2016**, *1*, 16152.
[3] J.-P. Correa-Baena, M. Saliba, T. Buonassisi, M. Grätzel, A. Abate, W. Tress, A. Hagfeldt, *Science* **2017**, *358*, 739.
[4] H. J. Snaith, *Nat. Mater.* **2018**, *17*, 372.
[5] NREL chart, http://nrel.gov/ncpv/images/efficiency_chart.jpg (accessed: August 2019).
[6] G. E. Eperon, T. Leijtens, K. A. Bush, R. Prasanna, T. Green, J. T.-W. Wang, D. P. McMeekin, G. Volonakis, R. L. Milot, R. May, A. Palmstrom, D. J. Slotcavage, R. A. Belisle, J. B. Patel, E. S. Parrott, R. J. Sutton, W. Ma, F. Moghadam, B. Conings, A. Babayigit, H.-G. Boyen, S. Bent, F. Giustino, L. M. Herz, M. B. Johnston, M. D. McGehee, H. J. Snaith, *Science* **2016**, *354*, 861.
[7] R. Lin, K. Xiao, Z. Qin, Q. Han, C. Zhang, M. Wei, M. I. Saidaminov, Y. Gao, J. Xu, M. Xiao, A. Li, J. Zhu, E. H. Sargent, H. Tan, *Nat. Energy* **2019**, *4*, 864.
[8] D. Zhao, Y. Yu, C. Wang, W. Liao, N. Shrestha, C. R. Grice, A. J. Cimaroli, L. Guan, R. J. Ellingson, K. Zhu, X. Zhao, R.-G. Xiong, Y. Yan, *Nat. Energy* **2017**, *2*, 17018.
[9] D. Zhao, C. Wang, Z. Song, Y. Yu, C. Chen, X. Zhao, K. Zhu, Y. Yan, *ACS Energy Lett.* **2018**, *3*, 305.
[10] D. Zhao, C. Chen, C. Wang, M. M. Junda, Z. Song, C. R. Grice, Y. Yu, C. Li, B. Subedi, N. J. Podraza, X. Zhao, G. Fang, R.-G. Xiong, K. Zhu, Y. Yan, *Nat. Energy* **2018**, *3*, 1093.
[11] J. Tong, Z. Song, D. H. Kim, X. Chen, C. Chen, A. F. Palmstrom, P. F. Ndione, M. O. Reese, S. P. Dunfield, O. G. Reid, J. Liu, F. Zhang, S. P. Harvey, Z. Li, S. T. Christensen, G. Teeter, D. Zhao, M. M. Al-Jassim, M. F. A. M. van Hest, M. C. Beard, S. E. Shaheen, J. J. Berry, Y. Yan, K. Zhu, *Science* **2019**, *364*, 475.
[12] C. Li, Z. Song, D. Zhao, C. Xiao, B. Subedi, N. Shrestha, M. M. Junda, C. Wang, C.-S. Jiang, M. Al-Jassim, R. J. Ellingson, N. J. Podraza, K. Zhu, Y. Yan, *Adv. Energy Mater.* **2019**, *9*, 1803135.
[13] W. Liao, D. Zhao, Y. Yu, N. Shrestha, K. Ghimire, C. R. Grice, C. Wang, Y. Xiao, A. J. Cimaroli, R. J. Ellingson, N. J. Podraza, K. Zhu, R.-G. Xiong, Y. Yan, *J. Am. Chem. Soc.* **2016**, *138*, 12360.
[14] W. Liao, D. Zhao, Y. Yu, C. R. Grice, C. Wang, A. J. Cimaroli, P. Schulz, W. Meng, K. Zhu, R.-G. Xiong, Y. Yan, *Adv. Mater.* **2016**, *28*, 9333.
[15] R. Prasanna, T. Leijtens, S. P. Dunfield, J. A. Raiford, E. J. Wolf, S. A. Swifter, J. Werner, G. E. Eperon, C. de Paula, A. F. Palmstrom, C. C. Boyd, M. F. A. M. van Hest, S. F. Bent, G. Teeter, J. J. Berry, M. D. McGehee, *Nat. Energy* **2019**, *4*, 939.
[16] A. F. Palmstrom, G. E. Eperon, T. Leijtens, R. Prasanna, S. N. Habisreutinger, W. Nemeth, E. A. Gaulding, S. P. Dunfield, M. Reese, S. Nanayakkara, T. Moot, J. Werner, J. Liu, B. To, S. T. Christensen, M. D. McGehee, M. F. A. M. van Hest, J. M. Luther, J. J. Berry, D. T. Moore, *Joule* **2019**, *3*, 2193.
[17] L. N. Quan, M. Yuan, R. Comin, O. Voznyy, E. M. Beauregard, S. Hoogland, A. Buin, A. R. Kirmani, K. Zhao, A. Amassian, D. H. Kim, E. H. Sargent, *J. Am. Chem. Soc.* **2016**, *138*, 2649.
[18] P. Gao, A. R. Bin Mohd Yusoff, M. K. Nazeeruddin, *Nat. Commun.* **2018**, *9*, 5028.
[19] D. Ramirez, K. Schutt, Z. Wang, A. J. Pearson, E. Ruggeri, H. J. Snaith, S. D. Stranks, F. Jaramillo, *ACS Energy Lett.* **2018**, *3*, 2246.

[20] E. H. Jung, N. J. Jeon, E. Y. Park, C. S. Moon, T. J. Shin, T.-Y. Yang, J. H. Noh, J. Seo, *Nature* **2019**, *567*, 511.
[21] Y. Lin, Y. Bai, Y. Fang, Z. Chen, S. Yang, X. Zheng, S. Tang, Y. Liu, J. Zhao, J. Huang, *J. Phys. Chem. Lett.* **2018**, *9*, 654.
[22] Z. Chen, M. Liu, Z. Li, T. Shi, Y. Yang, H.-L. Yip, Y. Cao, *iScience* **2018**, *9*, 337.
[23] Y. Liao, H. Liu, W. Zhou, D. Yang, Y. Shang, Z. Shi, B. Li, X. Jiang, L. Zhang, L. N. Quan, R. Quintero-Bermudez, B. R. Sutherland, Q. Mi, E. H. Sargent, Z. Ning, *J. Am. Chem. Soc.* **2017**, *139*, 6693.
[24] S. Shao, J. Liu, G. Portale, H.-H. Fang, G. R. Blake, G. H. ten Brink, L. J. A. Koster, M. A. Loi, *Adv. Energy Mater.* **2018**, *8*, 1702019.
[25] N. Aristidou, C. Eames, I. Sanchez-Molina, X. Bu, J. Kosco, M. S. Islam, S. A. Haque, *Nat. Commun.* **2017**, *8*, 15218.
[26] X. Xiao, J. Dai, Y. Fang, J. Zhao, X. Zheng, S. Tang, P. N. Rudd, X. C. Zeng, J. Huang, *ACS Energy Lett.* **2018**, *3*, 684.
[27] Q. Jiang, Y. Zhao, X. Zhang, X. Yang, Y. Chen, Z. Chu, Q. Ye, X. Li, Z. Yin, J. You, *Nat. Photonics* **2019**, *13*, 460.
[28] F. Wang, X. Jiang, H. Chen, Y. Shang, H. Liu, J. Wei, W. Zhou, H. He, W. Liu, Z. Ning, *Joule* **2018**, *2*, 2732.
[29] C. Fei, B. Li, R. Zhang, H. Fu, J. Tian, G. Cao, *Adv. Energy Mater.* **2017**, *7*, 1602017.
[30] R. Quintero-Bermudez, A. Gold-Parker, A. H. Proppe, R. Munir, Z. Yang, S. O. Kelley, A. Amassian, M. F. Toney, E. H. Sargent, *Nat. Mater.* **2018**, *17*, 900.
[31] Y. Yang, M. Yang, D. T. Moore, Y. Yan, E. M. Miller, K. Zhu, M. C. Beard, *Nat. Energy* **2017**, *2*, 16207.
[32] M. Yuan, L. N. Quan, R. Comin, G. Walters, R. Sabatini, O. Voznyy, S. Hoogland, Y. Zhao, E. M. Beauregard, P. Kanjanaboos, Z. Lu, D. H. Kim, E. H. Sargent, *Nat. Nanotechnol.* **2016**, *11*, 872.
[33] H. Tan, F. Che, M. Wei, Y. Zhao, M. I. Saidaminov, P. Todorović, D. Broberg, G. Walters, F. Tan, T. Zhuang, B. Sun, Z. Liang, H. Yuan, E. Fron, J. Kim, Z. Yang, O. Voznyy, M. Asta, E. H. Sargent, *Nat. Commun.* **2018**, *9*, 3100.
[34] M. Saliba, T. Matsui, J.-Y. Seo, K. Domanski, J.-P. Correa-Baena, M. K. Nazeeruddin, S. M. Zakeeruddin, W. Tress, A. Abate, A. Hagfeldt, M. Grätzel, *Energy Environ. Sci.* **2016**, *9*, 1989.
[35] S. J. Lee, S. S. Shin, Y. C. Kim, D. Kim, T. K. Ahn, J. H. Noh, J. Seo, S. I. Seok, *J. Am. Chem. Soc.* **2016**, *138*, 3974.
[36] I. Chung, J.-H. Song, J. Im, J. Androulakis, C. D. Malliakas, H. Li, A. J. Freeman, J. T. Kenney, M. G. Kanatzidis, *J. Am. Chem. Soc.* **2012**, *134*, 8579.
[37] X. Zheng, B. Chen, J. Dai, Y. Fang, Y. Bai, Y. Lin, H. Wei, X. C. Zeng, J. Huang, *Nat. Energy* **2017**, *2*, 17102.
[38] H. Tan, A. Jain, O. Voznyy, X. Lan, F. P. García de Arquer, J. Z. Fan, R. Quintero-Bermudez, M. Yuan, B. Zhang, Y. Zhao, F. Fan, P. Li, L. N. Quan, Y. Zhao, Z.-H. Lu, Z. Yang, S. Hoogland, E. H. Sargent, *Science* **2017**, *355*, 722.
[39] M. Stolterfoht, C. M. Wolff, Y. Amir, A. Paulke, L. Perdigón-Toro, P. Caprioglio, D. Neher, *Energy Environ. Sci.* **2017**, *10*, 1530.
[40] H. Zhou, Q. Chen, G. Li, S. Luo, T.-b. Song, H.-S. Duan, Z. Hong, J. You, Y. Liu, Y. Yang, *Science* **2014**, *345*, 542.
[41] M. Jørgensen, K. Norrman, F. C. Krebs, *Sol. Energy Mater. Sol. Cells* **2008**, *92*, 686.